Chapter 3

Degenerate Four Wave Mixing

3.1 Introduction

3.1.1 Theory of degenerate four-wave mixing

Frequency mixing represents one of the most general but nonetheless important phenomena in nonlinear optics. In this process, two or more waves interact in a nonlinear medium to produce an output at various sum or difference frequencies.

Four-wave mixing can take place in any material. It refers to the interaction of four waves via the third order nonlinear polarization. When all waves have the same frequency, the process is called degenerate, although their wavevectors are different. This process results from the nonlinear index of refraction.

Degenerate four-wave mixing (DFWM) can yield phase conjugation and is useful, for example, for correcting aberrations by using a phase conjugate mirror (PCM). To understand what phase conjugation is, consider an electric field $E_1(\mathbf{r},t) = \mathrm{Re}\{\psi(\mathbf{r})e^{i(kz-\omega t)}\}$, which has a spatial dependence $A_1(\mathbf{r}) = \psi(\mathbf{r})e^{ikz}$. If we can produce in the material another electric field $E_2(\mathbf{r},t) = \mathrm{Re}\{\psi^*(\mathbf{r})e^{i(-kz-\omega t)}\}$, with $A_2(\mathbf{r}) = \psi^*(\mathbf{r})e^{-ikz} = A_1^*(\mathbf{r})$ at any z, we call this field E_2 the *phase conjugate* of E_1. It can be thought of as the complex

conjugate of space but not time, or as a time-reversed wavefront. Now consider light that passes through an aberrating medium and becomes distorted. By reflecting the distorted wavefront off a phase-conjugate mirror, when the generated phase-conjugate wavefront passes back through the distorting medium, the output wave would be, ideally, undistorted.

As a technique, DFWM is one of those most heavily employed in characterizing third order nonlinear materials. There are several configurations that are used: folded boxcars, phase-conjugate or backward geometry, and two beam DFWM or forward geometry. The latter configuration is not phase matched. The working principle for all of these geometries is the following: two beams interfere to form some type of grating (e.g. intensity grating) and a third beam scatters off this grating, generating the fourth beam named the conjugate or signal beam.

The most frequently used DFWM configuration is the phase-conjugate geometry (fig. 3.1 (a)). In this configuration, two counter propagating pump beams, called backward (B) and forward (F), and a probe beam (P) are incident on the nonlinear material. Since beams B and F are collinear, $\mathbf{k}_F = -\mathbf{k}_B$. The probe beam is incident at a small angle θ to the direction of the forward beam. Due to the third order nonlinear polarization, a fourth beam is created and is referred to as the conjugate beam. This fourth beam is counterpropagating to the probe beam, $\mathbf{k}_C = -\mathbf{k}_P$. The process can be understood using the grating diagram (Figures 3.1 (b) and (c)). The forward and the probe beams interfere to form a grating from which the backward beam scatters, generating the conjugate beam. Similarly, the backward and probe beams create a grating from which the forward beam scatters and generates the conjugate beam.

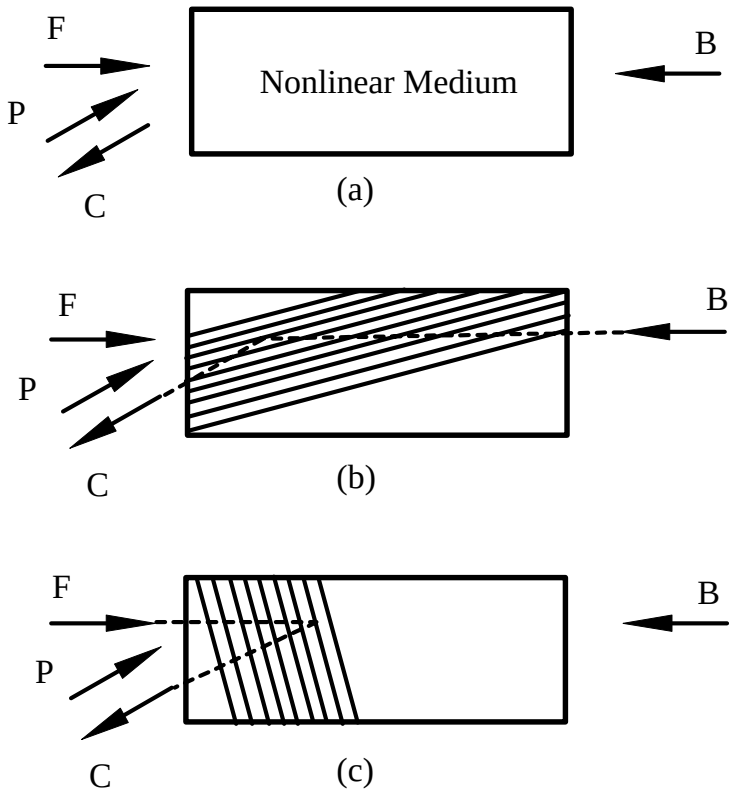

Fig. 3.1. a) Geometry and grating interpretation for phase-conjugation.

b) Backward beam scattering off grating created by forward and probe beams.

c) Forward beam scattering off grating formed by backward and probe beams.

We express the input fields as:

$$\mathrm{E}_i(\mathbf{r},\mathrm{t}) = \mathrm{A}_i(\mathbf{r})\mathrm{e}^{i(\boldsymbol{k}_i\cdot\boldsymbol{r}-\omega t)}\ ,\ \text{with i} = 1,2,3. \tag{1}$$

The nonlinear third-order polarization produced by the interaction of the three beams is oscillating at the same frequency ω as the input fields[1]:

$$\begin{aligned}\mathrm{P}_i^{(3)} &= 6\chi_{ijkl}^{(3)}(-\omega;\omega,\omega,-\omega)\mathrm{E}_j\mathrm{E}_k\mathrm{E}_l^* = \\ &= 6\chi_{ijkl}^{(3)}(-\omega;\omega,\omega,-\omega)\mathrm{A}_j\mathrm{A}_k\mathrm{A}_l^* e^{i(\boldsymbol{k}_1+\boldsymbol{k}_2-\boldsymbol{k}_3)\cdot\boldsymbol{r}}\end{aligned} \tag{2}$$

and is propagating in the $\mathbf{k}_1 + \mathbf{k}_2 - \mathbf{k}_3$ direction, where $\mathbf{k}_1$ and $\mathbf{k}_2$ correspond to the forward and backward beams and $\mathbf{k}_3$ corresponds to the probe beam. The subscripts j, k, and l correspond to the vector components of the forward, backward, and probe beams, respectively. Because the two pump waves are counterpropagating, their wavevectors are related by

$$\mathbf{k}_1 + \mathbf{k}_2 = 0, \tag{3}$$

and so, the nonlinear polarization expression becomes

$$\mathrm{P}_i^{(3)} = 6\chi_{ijkl}^{(3)}(-\omega;\omega,\omega,-\omega)\mathrm{A}_j\mathrm{A}_k\mathrm{A}_l^* e^{i(-\boldsymbol{k}_3)\cdot\boldsymbol{r}} \tag{4}$$

Therefore, the third order nonlinear polarization has a term in the spatial dependence part that allows it to act as a phase-matched term for a conjugate wave

(E_4) with a wavevector $-\mathbf{k}_3$. So we see that the probe and the conjugate waves are related by

$$\mathbf{k}_3 + \mathbf{k}_4 = 0. \tag{5}$$

The field amplitude of the wave generated by the nonlinear polarization is proportional to $A_j A_k A_l^*$ and is the phase conjugate of A_l.

3.1.2 Wave-equations for phase conjugation

The third order polarization expressed in the previous section couples the four interacting waves. Let us consider the counterpropagating pump beams as strong (undepleted), plane waves with slowly varying amplitudes A_i. Therefore, the second order derivative $\frac{d^2A_4}{dz^2}$ may be neglected $\left(\left|\frac{d^2A_4}{dz^2}\right| \ll \left|k_4 \frac{dA_4}{dz}\right|\right)$. This condition is valid as long as the fractional change in A_i over a distance of the order of the optical wavelength is much smaller than unity. The amplitude of the generated wave E_4 satisfies the wave equation:

$$\nabla^2 E_4 - \frac{\epsilon^{(1)}}{c^2}\frac{\partial^2 E_4}{\partial t^2} = \frac{4\pi}{c}\frac{\partial^2 P^{NL}}{\partial t^2} \tag{6}$$

where $P^{NL} = 6\chi^{(3)}(-\omega;\omega,\omega,\omega)E_1 E_2 E_3^*$ is the nonlinear source term.
Let $E_3(\mathbf{r},t) = A_3(z)e^{i(kz-\omega t)}$, and try a solution of the form $E_4(\mathbf{r},t) = A_4(z)e^{i(-kz-\omega t)}$. Substituting E_4 in the wave equation, where $\nabla^2 E_4(\mathbf{r},t) = \frac{d^2A_4}{dz2} - 2ik^2A_4 - A_4k^2$, and using the slowly varying amplitude approximation, we obtain:

$$\frac{dA_4}{dz} = -i\kappa A_3^* \tag{7}$$

and

$$\frac{dA_3}{dz} = i\kappa A_4^* \tag{8}$$

where

$$\kappa = \frac{12\pi\omega^3}{kc^2}\chi^{(3)}A_1A_2 \tag{9}$$

is called the coupling coefficient. To obtain the set of coupled equations above, it is assumed that θ, the angle between the probe and forward beam is very small. Otherwise, the left-hand sides of the equations should be multiplied by $\cos\theta$.

Using the boundary conditions $A_3(0) \neq 0$ and $A_4(L) = 0$, we obtain the solutions to the coupled wave equations:

$$A_3(z) = \frac{\cos[|\kappa|(z-L)]}{\cos(|\kappa|L)}A_3(0) \tag{10}$$

$$A_4(z) = -\frac{i\kappa}{|\kappa|}\frac{\sin[|\kappa|(z-L)]}{\cos(|\kappa|L)}A_3^*(0) \tag{11}$$

The output amplitudes of the two waves are:

$$A_3(L) = \frac{1}{\cos(|\kappa|L)}A_3(0) \tag{12}$$

$$A_4(0) = \frac{i\kappa}{|\kappa|}\tan(|\kappa|L)A_3^*(0) \quad (13)$$

The generated wave is therefore seen to be proportional to the complex conjugate of the input probe beam $A_3(0)$.

3.1.3 The intensity dependent refractive index (IDRI) and applications

The intensity dependent refractive index (IDRI) is defined as the change of the index of refraction due to the presence in a material of intense optical waves. As we have shown in Chapter 1, the expression for the intensity dependent refractive index is:

$$n = n_0 + n_2 I, \quad (14)$$

where n_0 is the linear index of refraction, n_2 is a constant, and I is the time-averaged intensity of the optical field. Because the intensity has units W/cm^2, the units used for n_2 are cm^2/W.

There are a variety of mechanisms that can cause the change in the index of refraction, and the applications of this effect are numerous as well.

Two important effects are a consequence of the IDRI: optical bistability and self-focusing (defocusing). In the case of optical bistability, the transmittance of an optical device, for example an optical cavity, may change from a low to a high value for a sufficiently high intensity and remains at this value until the intensity is reduced by a large amount. Such a device can be formed with a Fabry-Perot

interferometer containing a nonlinear medium. As can be seen in Figure 3.2, two output intensities are possible at a given input intensity. The device can be used as an optical memory element or as a switch in optical communication and in optical computing. If the input intensity is a given value I_b (with $I_l < I_b < I_h$), there are two possible output intensities. This situation corresponds to storing binary information. If a pulse of light is sent through the device, the system can make a transition to the higher state. If the input light is blocked momentarily, the system makes a transition to the lower state.

If the intensity of a light beam varies across its diameter, as is the case of Gaussian beams, than the refractive index of the material through which the beam propagates varies accordingly. Let us consider the case of the Gaussian beam. In the center of the beam the intensity is higher than at the edges. If $n_2 > 0$, the optical path length is larger in the center than at the edge, as is a converging lens. The beam is then focused as it is illustrated in Figure 3.3 (a). If $n_2 < 0$, then the beam path is larger at the edge, and the beam will defocus. In the case of self-focusing, if the nonlinear medium is short enough, the focusing will occur outside the medium, and therefore there is no potential for damaging the material. But if the nonlinear medium is long enough, the focusing occurs inside the material and damage may occur for input intensities that are high enough. Another interesting phenomenon that can take place inside a long nonlinear medium is the self-trapping of light. This takes place when the tendency of the beam to self-focus is compensated by its tendency to spread due to diffraction (see Figure 3.3 (b)). Then, the beam has a constant diameter over a relatively large distance inside the material. This process is unstable.

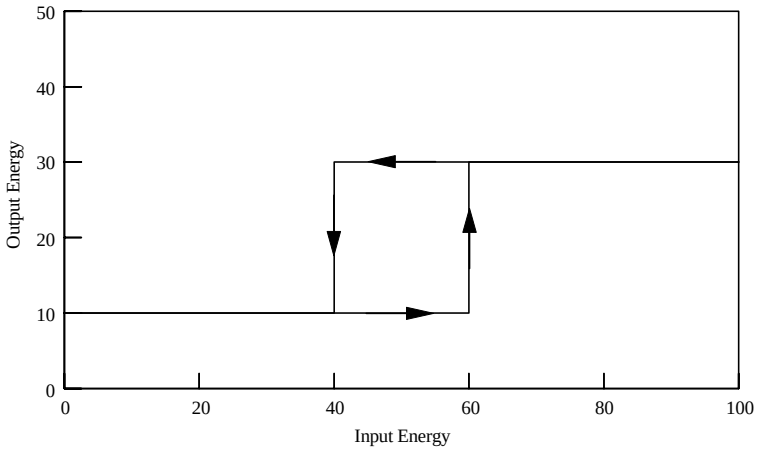

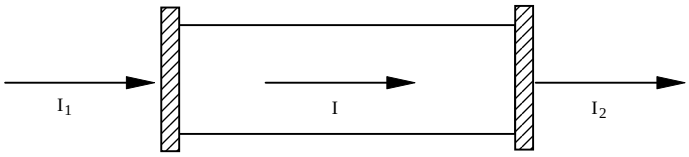

Fig. 3.2 a) An ideal characteristic for the input-output relation for a device that shows optical bistability; b) A bistable optical device consisting of a Fabry-Perot etalon containing a nonlinear medium.

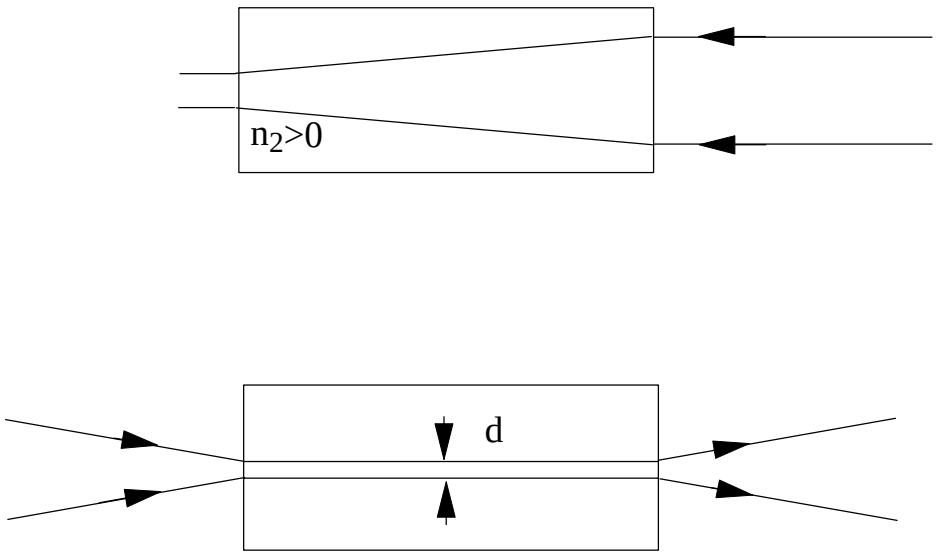

Fig. 3.3 a) Self-focusing of light. b) Self-trapping of light.

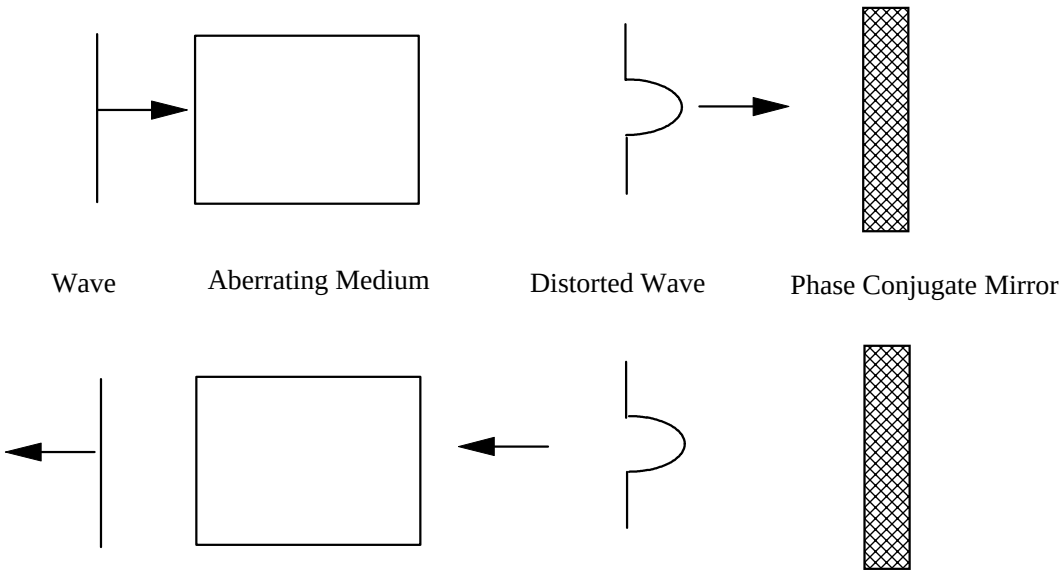

Fig. 3.4 The correction of a distorted wave is performed by reflecting the wave of a phase conjugate mirror, and passing the wave back through the distorting medium. The final wave is corrected for aberration.

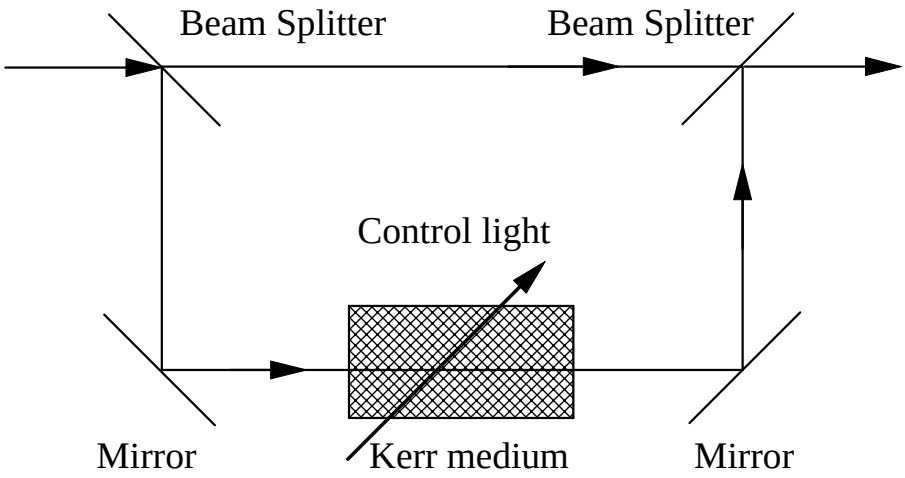

Fig. 3.5 The all-optical on-off switch is formed by a Mach-Zender interferometer which contains a Kerr material. By turning the control light on or off, the device output will be on or off.

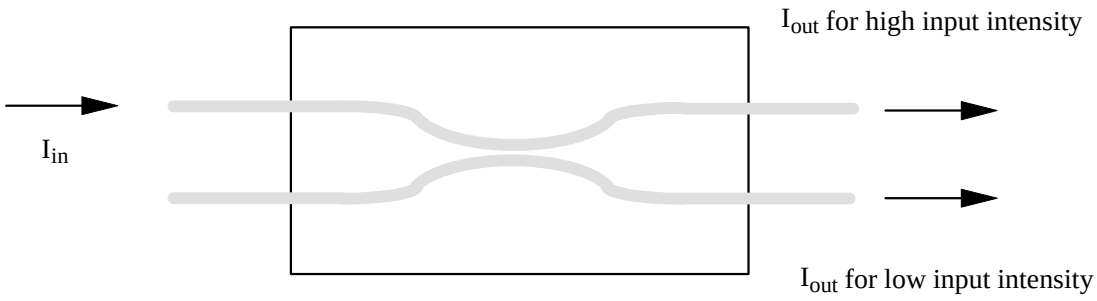

Fig. 3.6 The directional coupler is based on the intensity dependent refractive index. When the input intensity is low, the beam is redirected to the other waveguide, while for high input intensity the beam remains in the same waveguide.

Phase conjugation, which has been described in section 3.1.1 is used in the reconstruction of distorted waves, by reflecting the distorted wave with a phase-conjugate mirror and passing it through the same distorting medium. This is useful in optical resonators, where the distorted beams can be corrected by replacing one of the mirrors with a phase-conjugate mirror.

The development of fiber-optic communication and the potential of optical computing have led to increased interest in optical switches and optical couplers, mainly for their size, fast response, and low loss properties. The optical phase modulation in a Kerr medium can be used to modulate the intensity of light. By using the nonlinear medium in one arm of a Mach-Zender interferometer, for example, the transmittance of the interferometer can be turned on-off by turning on-off the controlling light, as illustrated in the Figure 3.5.

In a directional coupler, illustrated in Figure 3.6, only one beam of light is used to control its own transmission. By appropriate selection of the index of refraction and the dimensions of the device it is possible at low input intensity to redirect the beam to the other waveguide through coupling of the evanescent field. When the input beam intensity is high, due to the destruction of the coupling via the optical Kerr effect, the beam remains in the same waveguide. Such a device can be used to separate a sequence of weak and strong beams into the two outputs of the directional coupler.

3.1.4 Grating formation and types of gratings

In terms of the intensity dependent refractive index, the DFWM process is considered as the interference of two input beams which results in a grating

formation from which the third beam scatters generating the phase-conjugate wave. This is because the interference results in a spatially periodic light intensity or distribution of polarization. As a result, the optical properties of the material are changed, with the grating represented by the spatial modulation of these parameters. The type of grating created depends on the properties of the medium as well as the characteristics of the input beams.

For highly absorptive materials, for example, an incident laser beam populates the excited electronic states due to the absorption of light. Therefore, a **population density grating** is created. During the relaxation of the excited states, a **space charge grating** can form if there are excited, mobile charges. Space charge gratings are important in photorefractive materials, for example. During the absorption process, heat is created in regions of high optical intensities and therefore a *temperature grating* is formed. The material tends to expand in these regions generating *stress, strain,* and *density gratings*, and in mixtures it can be accompanied by *concentration gratings*[(2)]. Various time-dependent studies of the phase-conjugate signal can give information on the different relaxation mechanisms in the nonlinear medium and their characteristic parameters. These latter five gratings are included in one large category generally known as the **thermal grating**. The response time for the thermal grating is approximately 10^{-3}s[(1)].

Another type of grating is the **orientational grating**, which forms on time scales of 10^{-12} s. It is a result of the alignment of anisotropic molecules to the electric field when an optical wave is applied.

Nonresonant electronic nonlinearities (resulting strictly from the redistribution of the electrons in the medium) are very fast, since they involve only virtual

processes[1]. The time necessary for **electronic gratings** to form is very short, $< 10^{-15}$ s, which is the time required for an electron cloud to become distorted in response to an applied optical field.

For this study we are interested only in the electronic contribution to the nonlinear susceptibility $\chi^{(3)}$ because of its inherently fast response. We can separate it from the other mechanisms by using different polarizations of the input beams[3,4], i.e. the probe beam has a polarization orthogonal to the pump beams. In this configuration, the intensity grating is absent, and the only grating formed in the material is the polarization grating. That is, the interference results in a spatially uniform intensity but a periodic variation in the direction of the optical electric field. Since the intensity is uniform, population and thermal gratings do not exist in this configuration.

3.1.5 DFWM experimental configuration

DFWM is a useful technique for characterizing third order nonlinear materials.

In general, the intensity of the phase-conjugate signal I_s is represented by the following expression:

$$I_s = a' I_b I_f I_p \,, \tag{15-a}$$

where I_b is the intensity of the backward beam, I_f is the intensity of the forward beam, I_p is the intensity of the probe and a' is a constant that contains the third order nonlinear susceptibility.

The input pump beams, I_b and I_f, are considered to be of equal intensity, I_0. Since the experimental configuration is in such a way that $I_p = \text{const.} \times I_0$, the dependence is cubic with respect to I_0,

$$I_s = aI_0^3 \tag{15-b}$$

The data obtained from the measurements is fitted to an equation of the above form. Using the least-squares fit method, the value for the coefficient a can be determined. The third order nonlinear susceptibility, $\chi^{(3)}$ is proportional to the value of the coefficient a. The same technique can be then employed for a standard material with a known value for $\chi^{(3)}$, which can be used as a reference for the measurements. CS_2, for example, was used as a reference in this work. The data analysis for the reference material is the same as is used for the sample and yields the value for the coefficient a_{ref}. Then, the value for $\chi^{(3)}$ is given by the formula[5]:

$$\chi^{(3)}_{eff} = \left(\frac{n_0}{n_{ref}}\right)^2 \left(\frac{L_{ref}}{L}\right) \left(\frac{a}{a_{ref}}\right)^{\frac{1}{2}} \chi^{(3)}_{ref}, \tag{16}$$

where n_0, n_{ref} are the refractive indices for the sample and reference respectively, L is the sample thickness, and $\chi^{(3)}_{ref}$ is the third order nonlinear susceptibility for the reference.

This technique allows only for the modulus of $\chi^{(3)}$ to be found, but one advantage in the case of isotropic materials is that all components of the tensor $\chi^{(3)}$ can be determined, using different polarizations for the input beams.

The third order susceptibility tensor $\chi^{(3)}_{ijkl}$ is a fourth-rank tensor with 81 elements. For isotropic media, it has 21 nonzero components, of which only 3 are independent[(1)]:

$$\chi^{(3)}_{yyzz} = \chi^{(3)}_{zzyy} = \chi^{(3)}_{zzxx} = \chi^{(3)}_{xxzz} = \chi^{(3)}_{xxyy} = \chi^{(3)}_{yyxx} \tag{17-a}$$

$$\chi^{(3)}_{yzyz} = \chi^{(3)}_{zyzy} = \chi^{(3)}_{zxzx} = \chi^{(3)}_{xzxz} = \chi^{(3)}_{xyxy} = \chi^{(3)}_{yxyx} \tag{17-b}$$

$$\chi^{(3)}_{yzzy} = \chi^{(3)}_{zyyz} = \chi^{(3)}_{zxxz} = \chi^{(3)}_{xzzx} = \chi^{(3)}_{xyyx} = \chi^{(3)}_{yxxy} \tag{17-c}$$

and

$$\chi^{(3)}_{xxxx} = \chi^{(3)}_{yyyy} = \chi^{(3)}_{zzzz} = \chi^{(3)}_{xxyy} + \chi^{(3)}_{xyxy} + \chi^{(3)}_{xyyx} \tag{17-d}$$

The above expressions can be put in a general form:

$$\chi^{(3)}_{ijkl} = \chi^{(3)}_{xxyy}\delta_{ij}\delta_{kl} + \chi^{(3)}_{xyxy}\delta_{ik}\delta_{jl} + \chi^{(3)}_{xyyx}\delta_{il}\delta_{jk} \tag{18}$$

For nonresonant electronic response, the components of the nonlinear susceptibility tensor are:

$$\chi^{(3)}_{xxxx} = 2\chi^{(3)}_{xxyy} + \chi^{(3)}_{xyyx} \tag{19}$$

Using the Kleinman symmetry condition for low-frequency optical fields, the above relation becomes:

$$\chi^{(3)}_{xxyy} = \chi^{(3)}_{xyxy} = \chi^{(3)}_{xyyx} = \tfrac{1}{3}\chi^{(3)}_{xxxx} \tag{20}$$

In this thesis, we determine the value of $\chi^{(3)}_{xyyx}$, with the probe beam p-polarized (horizontal polarization) and the pump beams s-polarized (vertical polarization).

One necessary correction in relating the molecular susceptibility to the value for the macroscopic third order nonlinear susceptibility is the local field factor[1]. This is due to the difference between the applied macroscopic electric field and the effective electric field, or Lorentz local field, that each atom or molecule experiences. In the nonlinear-optical case, the Lorentz local field is given by:

$$\mathbf{E}_{\text{loc}} = \mathbf{E} + \tfrac{4\pi}{3}\mathbf{P}\,, \tag{21}$$

where the polarization **P** has both linear and nonlinear contributions included, i.e.

$$\mathbf{P} = \mathbf{P}^{\text{L}} + \mathbf{P}^{\text{NL}} \tag{22}$$

Following the procedure described in Reference 1, the third order nonlinear susceptibility becomes:

$$\chi^{(3)}_{ijkl}(-\omega;\omega,\omega,-\omega) = \left(\tfrac{n^2+2}{3}\right)^4 \text{N}\gamma_{ijkl}(-\omega;\omega,\omega,-\omega), \tag{23}$$

where the term $\frac{n^2+2}{3} = \text{f}$, represents the local-field correction.

3.1.6 Effects of linear nonresonant absorption

Although the DFWM measurements for this thesis are made away from resonance, there is a small background absorption. To account for this effect, the third order nonlinear susceptibility must be corrected for absorption[6]:

$$\chi^{(3)}_{\text{eff}} = \left(\frac{n_0}{n_{\text{ref}}}\right)^2 \left(\frac{L_{\text{ref}}}{L}\right) \left(\frac{a}{a_{\text{ref}}}\right)^{\frac{1}{2}} \frac{\alpha L \exp(\alpha L/2)}{1-\exp(-\alpha L)} \chi^{(3)}_{\text{ref}} , \tag{24}$$

where α is the absorptivity of the sample.

3.2 Properties of endohedral metallofullerenes

Of particular interest among the fullerenes are the endohedral metallofullerenes, in which a small number of metal atoms (one to three) resides inside the fullerene molecular cage. Fullerenolanthanides are "new kinds of organolanthanide compounds stabilized by the delocalization of the negative charges on the fullerene cages and the protection of the lanthanide metals by spherical carbon ligands"[7]. Besides the endohedral fullerenes with rare-earth atoms inside, (e.g. La@C_{82}, Er_2@C_{82}, Tm_2@C_{82}, Sc_2@C_{84}, Sc_3@C_{82}, etc.) other species have been also synthesized[8] (e.g. U@C_{28}, U_2@C_{60}, Ca@C_{60}, Fe@C_{60}, alkali fullerenes, noble gas fullerenes, etc.).

The structure and composition of these materials suggest some extremely important properties regarding nonlinear optics: charge transfer of electrons from

the metal to the fullerene cage and new long-wavelength optical absorption features.

Early studies on these materials were limited to just a few methods, such as electron paramagnetic resonance (EPR), laser desorption time of flight mass spectroscopy (LD-TOF)[9] and linear spectroscopy. The difficulty in analyzing these materials came mainly from very small production yields (on the order of hundreds micrograms), and the difficulties encountered in the processes of separation and purification. Nonetheless, the importance of these studies was to identify the materials synthesized and to prove that the metal atoms are encapsulated inside the cage and that the charge transfer occurs.

Electron paramagnetic resonance (EPR) measurements of several endohedral metallofullerenes have proven the charge transfer of electrons from the internal metal atom to the fullerene cage. For La@C_{82}, the La atom is found to be in the +3 oxidation state[10]. Also, EPR measurements for Sc@C_{82} and Sc_3@C_{82} showed that the Sc atom's oxidation state inside the cage is $+3$[11] and that the three Sc encapsulated atoms are equivalent.

Scanning tunneling microscopy (STM) images[8] of metallofullerenes Sc@C_{74} and Sc_2@C_{74} on a silicon surface show the molecules to be spherical with cage diameters of ~ 9.5 Å. High-resolution TEM images from Sc_2@C_{84} crystal[12] lead to the conclusion that the scandium atoms are inside the carbon cage, which has a diameter of ~8.4 Å. Intermolecular spacing measurements in Sc_2@C_{84} and C_{84} indicate that the charge transfer to the cage in Sc_2@C_{84} does not significantly increase the size of the carbon cage.

Fluorescence measurements in Er_2@C_{82} showed emission at 1.5 µm, typical for $^4I_{13/2} \rightarrow {}^4I_{15/2}$ transitions of Er^{3+}[13,14], thus indicating that the endohedral

metal atoms are trivalent in this case as well. Studies on crystalline rare earths[15] have concluded that sharp-line absorption comes from forbidden transitions within the 4f shell. All rare earths elements have an open 4f shell and most of them form trivalent ions. The properties of the trivalent ions are therefore more important even than those of the neutral atoms, as in the cases of the Nd^{3+}:YAG laser and in Er^{3+}-doped optical fiber amplifiers, for example.

The charge-transfer from dopant atoms to the fullerene cage can be considered similar to the effect of optical excitation of the corresponding empty cage fullerene. That is, electrons are placed into the lowest unoccupied molecular orbital (LUMO), although there are no holes produced in the highest occupied molecular orbital (HOMO) as there are in the case of optical excitation. This analogy is particularly important because optical excitation has been shown both theoretically and experimentally to produce orders of magnitude enhancement in the $\chi^{(3)}(-\omega_4;\omega_1,\omega_2,\omega_3)$ of simple conjugated organic molecules. Third harmonic generation (THG)[16] measurements of a naphthalocyanine and DFWM[17,18] measurements of a linear polyene, both demonstrated the $\chi^{(3)}$ enhancement due to optical excitation.

The THG experiment was performed on dilute solutions of silicon naphthalocyanine (SINC). The solutions of SINC were optically pumped in the Q-band at 770 nm and then probed by 30 ps pulses at 1543 nm. The THG Maker fringe amplitude was observed to decrease significantly because of the large and negative second order hyperpolarizability, $\gamma^{S_1}(-3\omega;\omega,\omega,\omega)$, of the first excited state of SINC. This value, of $(1064 \pm 100) \times 10^{-36}$ esu, is orders of magnitude larger than the second order hyperpolarizability, $\gamma^{S_0}(-3\omega;\omega,\omega,\omega)$ ($< 10 \times 10^{-36}$ esu) of the ground state.

The DFWM experiment used the forward geometry, with two orthogonally polarized 1064 nm probe beams and a 355 nm pump beam, with a pulsewidth of 30 ps. The 355 nm pump beam excites diphenylhexatriene (DPH), in solution, to its first optical excited state. Because this state is populated for times on the nanosecond scale, it is possible to perform nonresonant measurements of $\chi^{(3)}(-\omega_4;\omega_1,\omega_2,\omega_3)$ at frequencies different from the resonant pump frequency, by using picosecond probe pulses. An increase of the 1064 nm DFWM signal by a factor of 100 was observed when the 355 nm pump was turned on, compared to the situation when the pump beam was turned off.

These experiments both showed that the optical nonlinearities of conjugated organic materials can be enhanced by orders of magnitude when the material is brought into the excited state. While $\chi^{(3)}$ is greatly enhanced, it also requires a strong pump beam and then it rapidly decays when the pump beam is turned off. Therefore it would be desirable to have a material with a ground state that resembles the excited state. This condition is satisfied in the case of the endohedral metallofullerenes, in which the charge-transfer that occurs from the encapsulated atom(s) to the fullerene cage represents a good simulation of the optical excitation of the corresponding empty cage fullerene.

Therefore the endohedral metallofullerenes were anticipated to show enhancement of NLO properties (i.e. ground state $\chi^{(3)}$) without optical excitation of the material. Furthermore, previous studies of empty cages C_{60} and C_{70} demonstrated that these materials already possess relatively large third order susceptibilities $\chi^{(3)}(-\omega_4;\omega_1,\omega_2,\omega_3)$, on the order of 10^{-11} esu[19,20]. Our DFWM measurements on solutions of the endohedral metallofullerene $Er_2@C_{82}$ show that

the mechanism of charge-transfer from metal to cage, in fact, produces an enhancement in $\chi^{(3)}$ by two orders of magnitude.

3.3 Experimental configuration and materials

A. Experimental configuration

The measurements were done using the standard phase-conjugate (backward) geometry described in section 3.1.1. Figure 3.7 displays the experimental configuration, where the input beam is the fundamental 1064 nm wavelength of a Q-switched Nd:YAG laser, with a pulse width of 15 ns. This beam is divided by beam splitters (BS) so that the two pump beams have the same maximum energy of 3 mJ (intensity of 33 MW/cm^2) and the probe's energy is 1 mJ. The two counter-propagating pump beams intersect with the probe beam at an angle of 5° inside the sample. The value for the probe angle was chosen as small as possible in order to maximize the overlapping region of the beams inside the sample cell. All three beams have approximately the same path length from the laser to the sample of 2.3 m, so that they also temporally overlap to generate the phase conjugate beam. There are two conditions required for the thickness of the sample, L, that need to be satisfied in order to have a complete overlapping inside the sample cell:

$$L < ct_{FWHM} \qquad \text{and} \qquad L < \frac{2w}{\sin\theta}$$

where t_{FWHM} is the full width at half-maximum temporal pulsewidth of the laser and θ is the angle between the probe and the forward beam. The first condition ensures that the temporal overlapping of the beams takes place throughout the

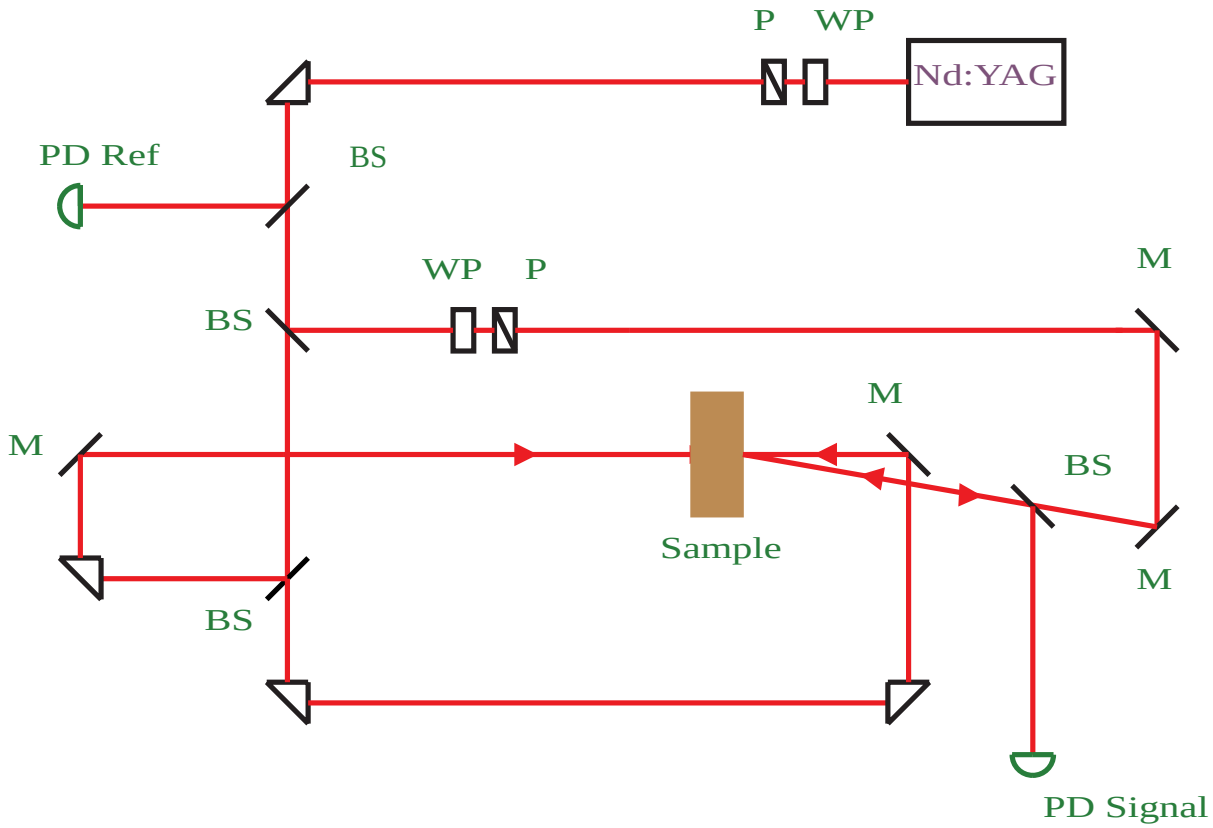

Fig. 3.7 DFWM experimental configuration

sample cell. The second condition sets a limit on the sample thickness, where 2w is the diameter of each of the beams intersecting at an angle θ inside the sample, as shown in Figure 3.8. For this experiment both conditions are met, since L = 5 mm, $c \cdot t_{FWHM} = 4.5$ m, and $2w/\sin\theta = 6.8$ mm. The beams are relatively well collimated inside the sample using lenses with long focal length. A 2 m focal lens was used for the pumps and a 1 m focal lens for the probe beam. Although a very difficult and time consuming procedure, it is very important to have the pump beams precisely counterpropagating so that the phase-conjugate signal can be generated. One way to check the counterpropagation is to verify that the pump beams overlap at three different points along their direction of propagation. This is done by translating a 50 μm pinhole across the beams and recording the beam profile for each of the beams. When necessary, alignment is performed by adjusting the orientation of the final mirrors. The same pinhole is used to measure the beam profile at the sample location where all three beams should overlap. Inside the sample all three beams are focused to $\frac{1}{e^2}$ radii of approximately 500 μm and all have a gaussian profile as seen in Figures 3.9-3.14. The polarization of the probe is perpendicular to the polarization of the pump beams, in order to eliminate the thermal and population grating as described in Section 3.1.4. Therefore, the phase-conjugate wave, which is counter-propagating with respect to the probe beam, also has a polarization orthogonal to that of the pumps. A beamsplitter (BS) is used to separate the conjugate beam from the probe and to direct it towards a large area silicon photodiode (PD). In front of the PD is a low power polarizer whose axis of polarization is kept parallel to the polarization direction of the conjugate beam. This allows the PD to detect only the conjugate signal and eliminates any scattered light from the pumps and the rest of the optics from

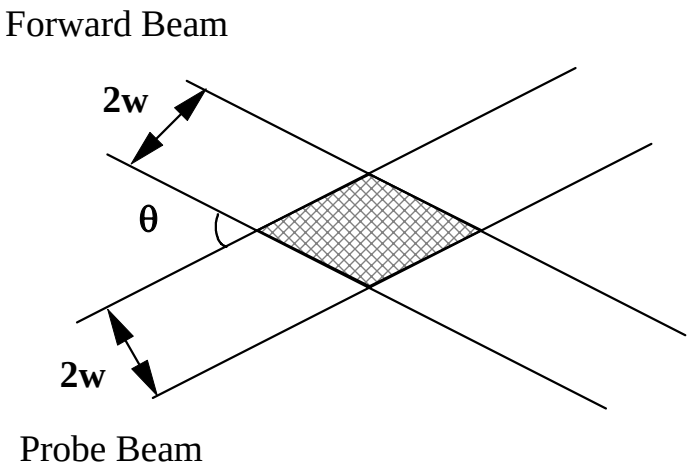

Fig. 3.8. The sample thickness, L, is determined by the relation $L < \frac{2w}{\sin\theta}$.

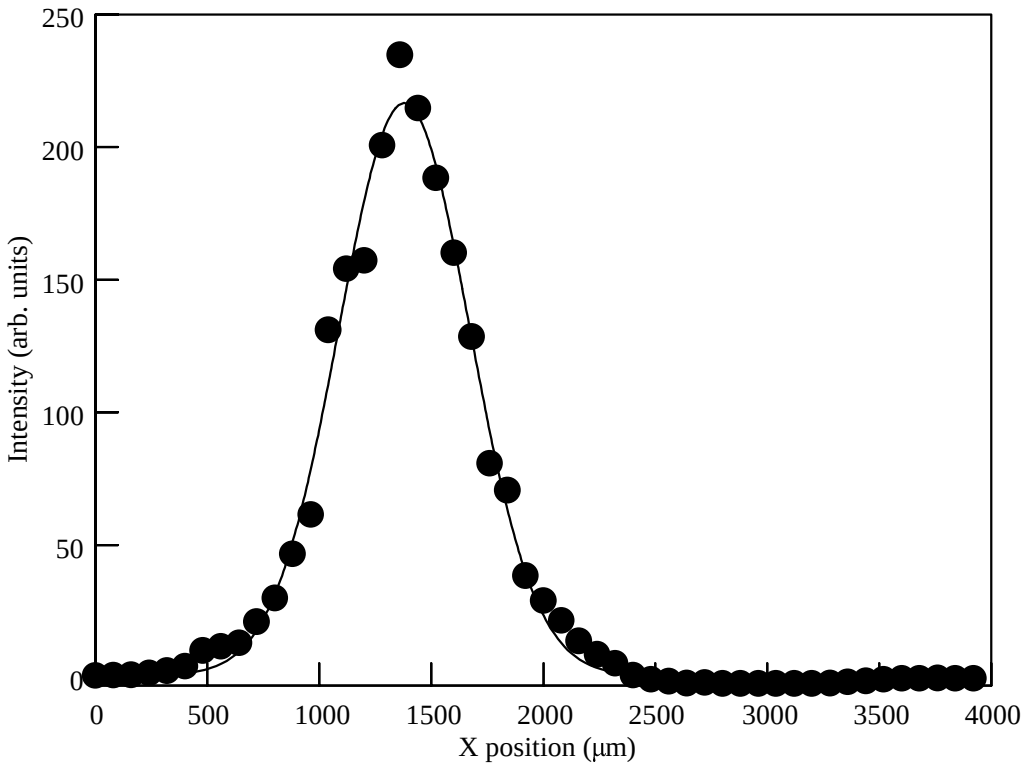

Fig. 3.9 Horizontal beam scan for the forward (F) beam at 1064 nm.

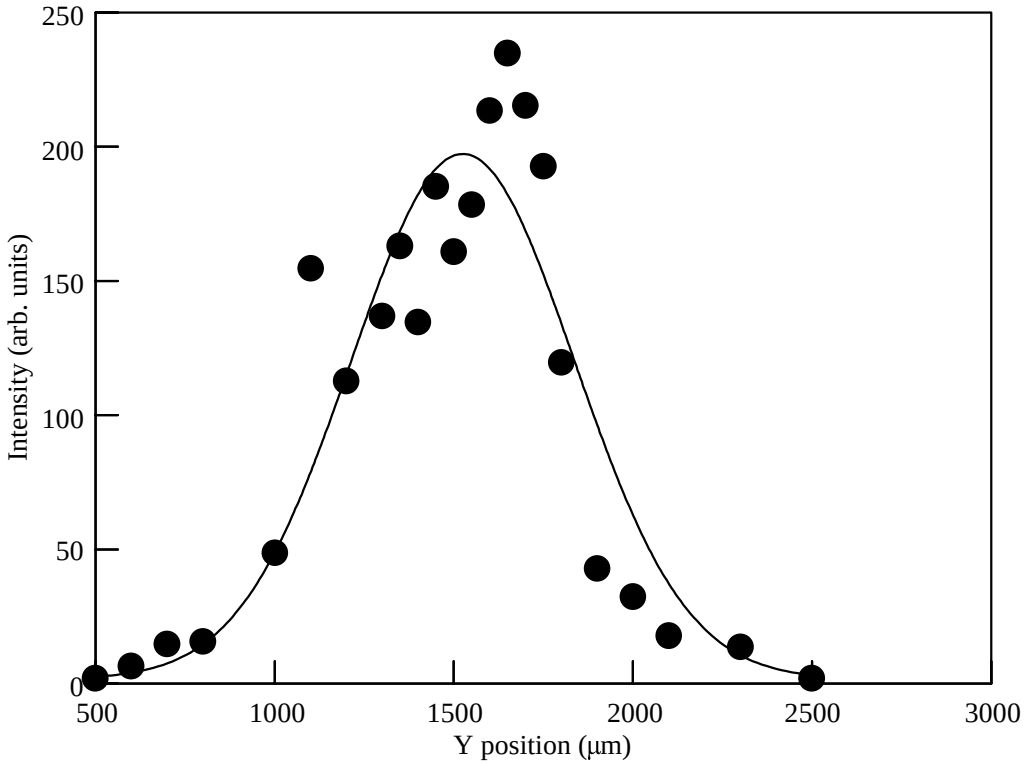

Fig. 3.10 Vertical scan for forward (F) beam at 1064 nm.

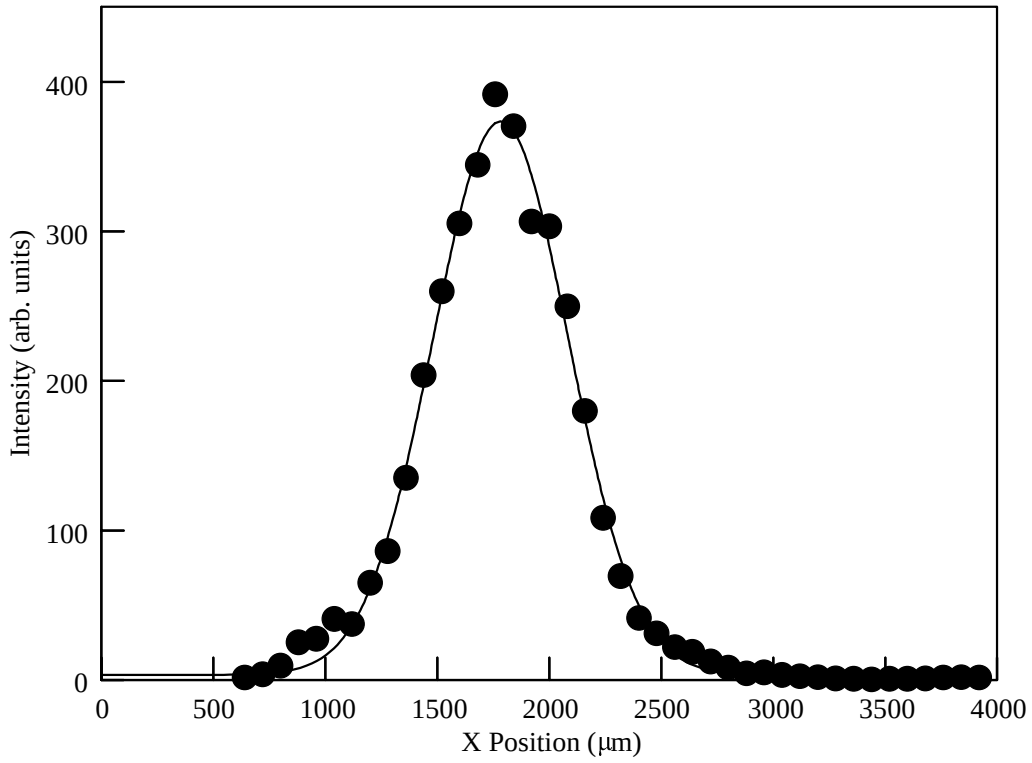

Fig. 3.11 Horizontal scan for backward (B) beam at 1064 nm.

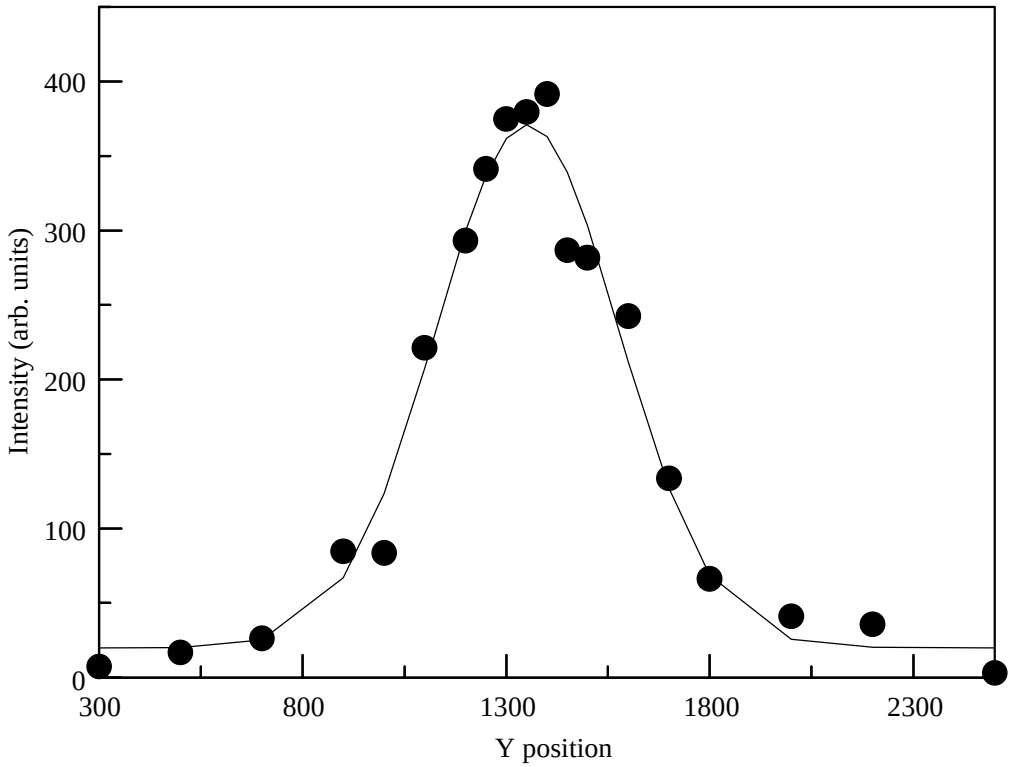

Fig. 3.12 Vertical scan for backward (B) beam at 1064 nm.

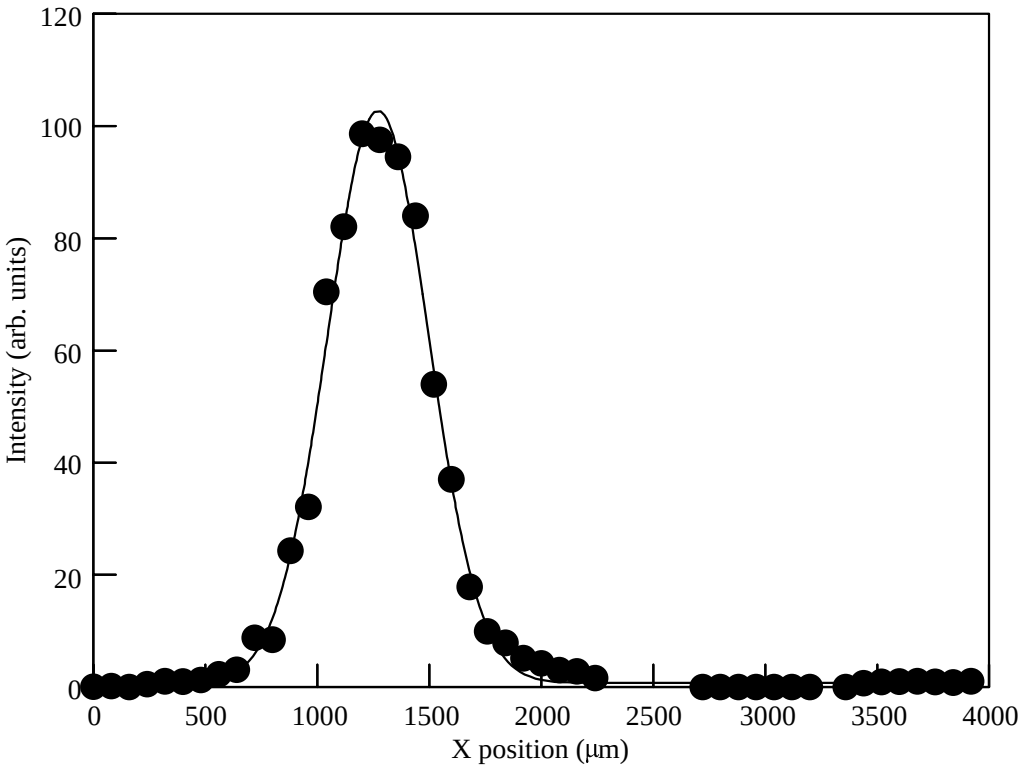

Fig. 3.13 Horizontal scan for probe (P) beam at 1064 nm.

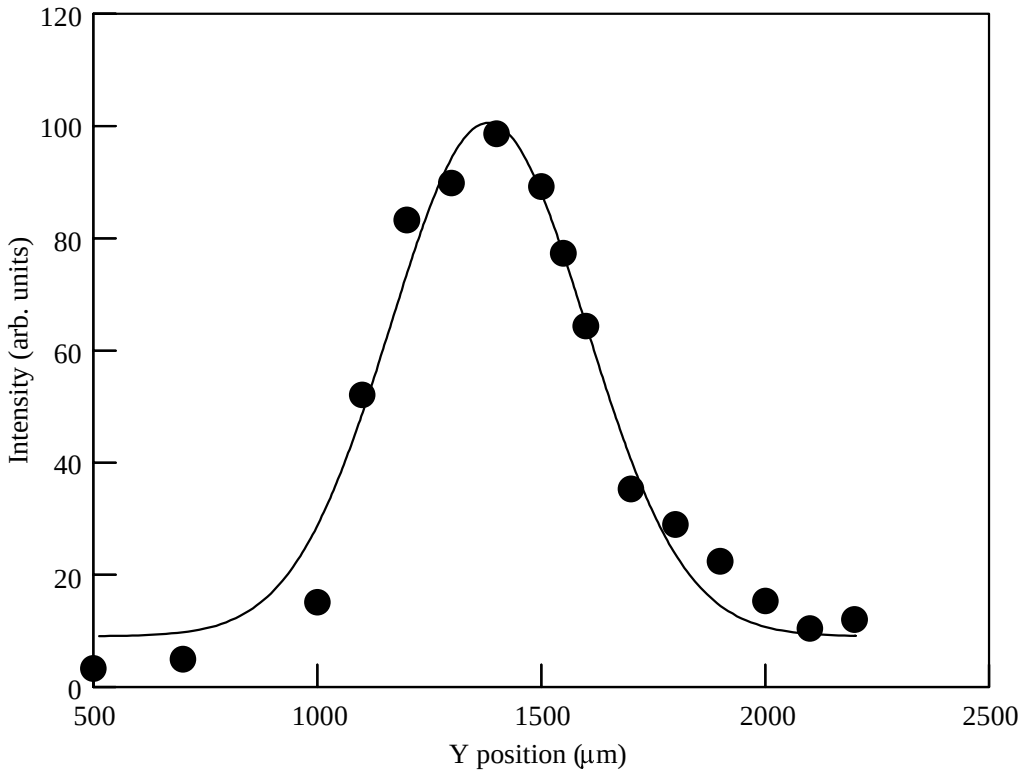

Fig. 3.14 Vertical scan for probe (P) beam at 1064 nm.

reaching the PD. The PD is connected to an analog-to-digital converter (ADC) in a CAMAC crate. Each measurement is made by averaging over 100 laser pulses. The background due to any scattering from the optics is automatically subtracted by the computer before every experimental run. The input intensity is varied with a combination of a half waveplate and a Glan-Taylor polarizer. Part of the incident beam is send by a BS to a reference large area photodiode, and the intensity recorded is proportional to the input intensity. We have to be careful with the back reflection of the pump beams so that they do not retrace back into the laser crystal which could then be damaged in this way.

Each measurement consists of recording the output intensity of the conjugate signal vs. the input intensity. For each different concentration of the solution this is done for the reference as well as for the solution studied. The solutions are contained in 5 mm path length Bk 7 glass spectrophotometer cells. For each concentration the linear absorption coefficient is also measured for use in Eq. 24.

B. Materials

The materials were generously provided by the group of Prof. Harry Dorn from the Department of Chemistry at Virginia Tech. The samples were separated and purified using an automated high performance liquid chromatography (HPLC) apparatus[9]. This method yields multi-miligram quantities of the endohedral metallofullerenes. The initial soot containing the endohedral metallofullerene was obtained using the Kratschmer-Huffman electric arc burning method on cored rods containing a graphite/metal-oxide mixture. The soot contains empty cage fullerenes as well as the endohedral metallofullerenes $Er@C_{82}$ and three isomers of $Er_2@C_{82}$. The $Er_2@C_{82}$ isomer mixture is separated in a multistep automated

HPLC procedure that utilizes Buckyclutcher and Pentabromobenzyl (PBB) derivatized silica gel columns. The addition of the PBB chromatographic step in the separation process allows for automation of the separation process, in contrast with previous procedures. Mass spectroscopy measurements show three distinct fractions for $Er_2@C_{82}$, indicating the presence of three isomers for this structure. They are further separated by passing the mixture through a final Buckyclutcher column. The overall yield of $Er_2@C_{82}$ is more than 1% of the initial endohedral metallofullerene mixture. The material used for degenerate four-wave mixing experiments is identified as $Er_2@C_{82}$ isomer III.

Although initially we had a large variety of samples in solution form, due to very low concentrations we could only obtain the absorption spectra, but not the DFWM measurements for several materials. These are shown in Figures 3.15-3.19, for $Er_2@C_{82}$, $Er_2@C_{84}$, $Er_2@C_{90}$, $Sc_2@C_{84}$, $Tm_2@C_{82}$, as well as the empty cages C_{82}, and C_{84}. DFWM measurements were performed only on the $Er_2@C_{82}$ isomer III and C_{82} solutions in CS_2. Other solvents have been tried such as toluene, methanol, benzene, dichlorobenzene, and acetone, but $Er_2@C_{82}$ had a substantially lower solubility in these solvents than in CS_2.

The initial concentration of $Er_2@C_{82}$ (isomer III) solution in CS_2 was 3×10^{-4} M/l. Each time the solution had to be diluted it was done in a DRI-LAB glove box (from Inert Atmosphere and Vacuum Deposition Equipment) which provides a moisture and oxygen-free atmosphere by circulating an inert gas (N) inside the glove box. This is necessary because of the CS_2 solvent which is sensitive to moisture and oxygen contamination. The solution was sonicated at room temperature in a Bransonic® Ultrasonic Cleaner 2200 from Branson. After each dilution, we measured the absorption spectrum of the solution with a UV/IR Jasco

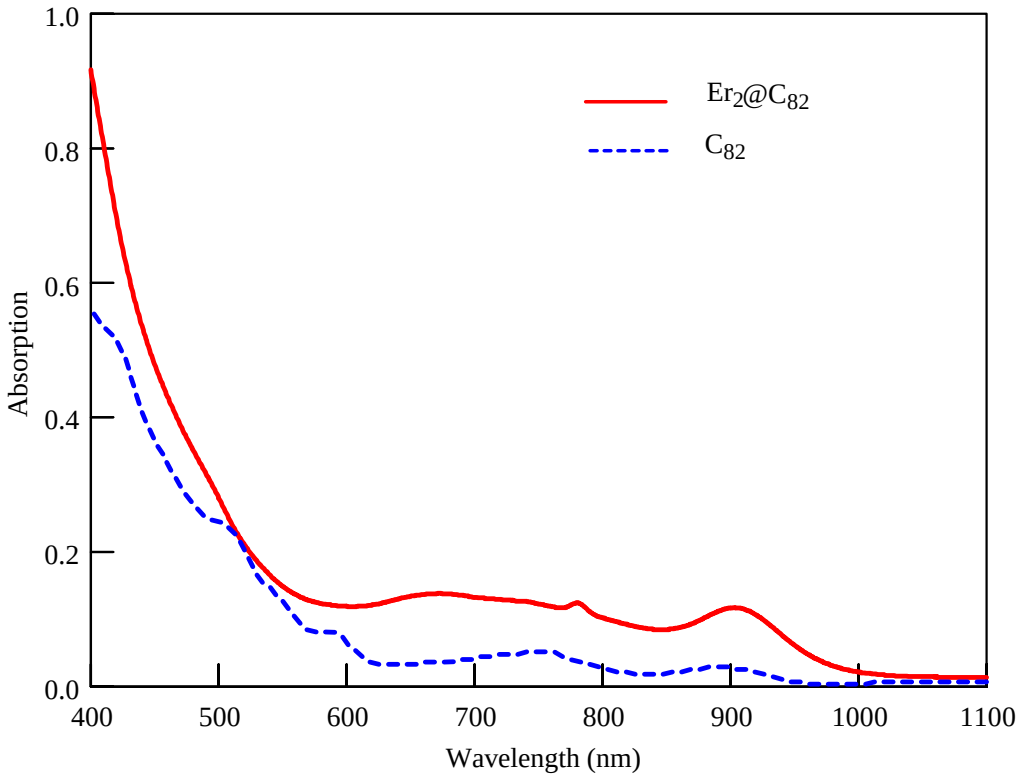

Fig. 3.15 Absorption spectra for $Er_2@C_{82}$ and C_{82} solutions in CS_2.

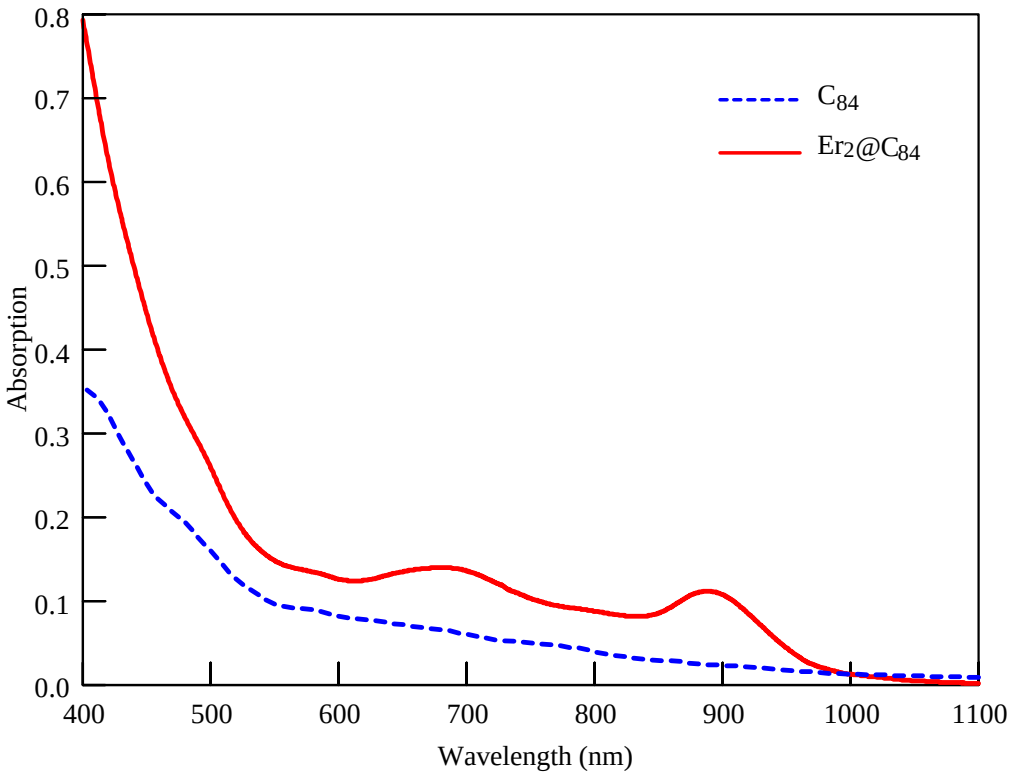

Fig. 3.16 Absorption spectra for $Er_2@C_{84}$ and C_{84} solutions in CS_2.

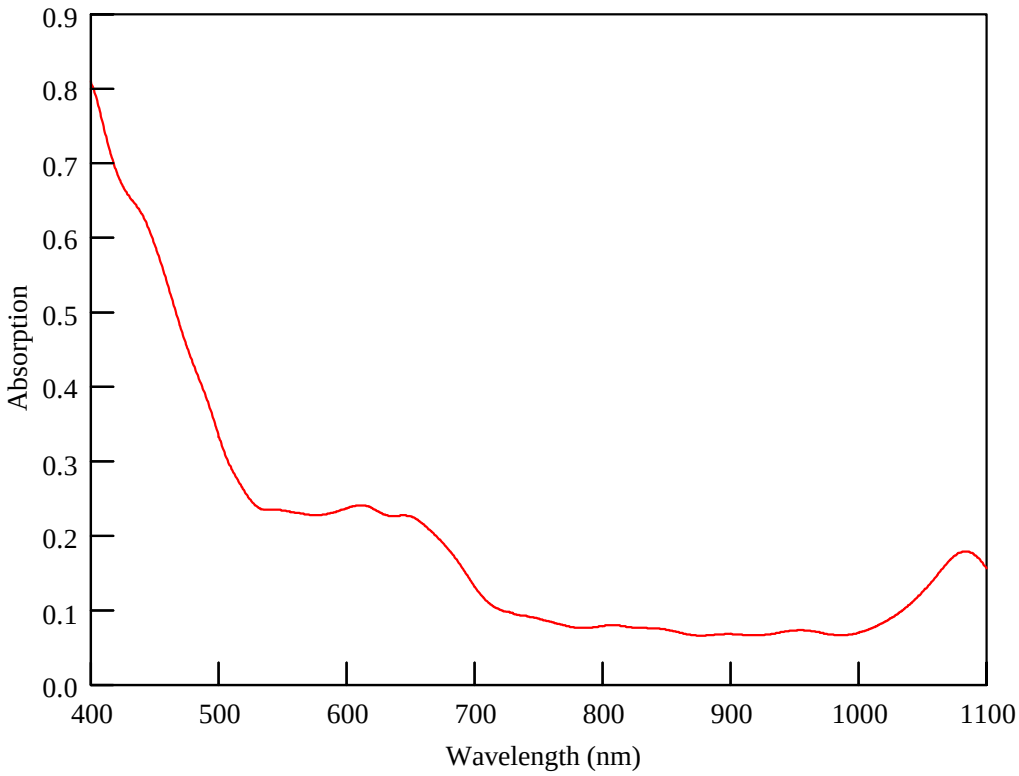

Fig. 3.17 Absorption spectrum for $Er_2@C_{90}$ solution in CS_2.

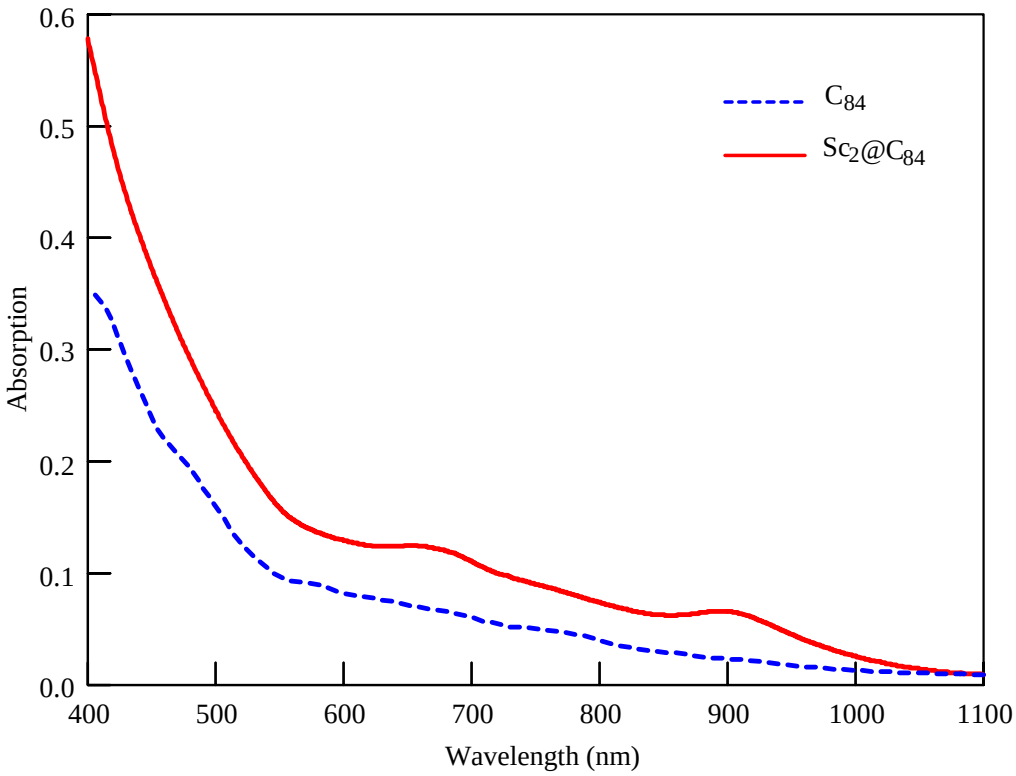

Fig. 3.18 Absorption spectra for $Sc_2@C_{84}$ and C_{84} solutions in CS_2.

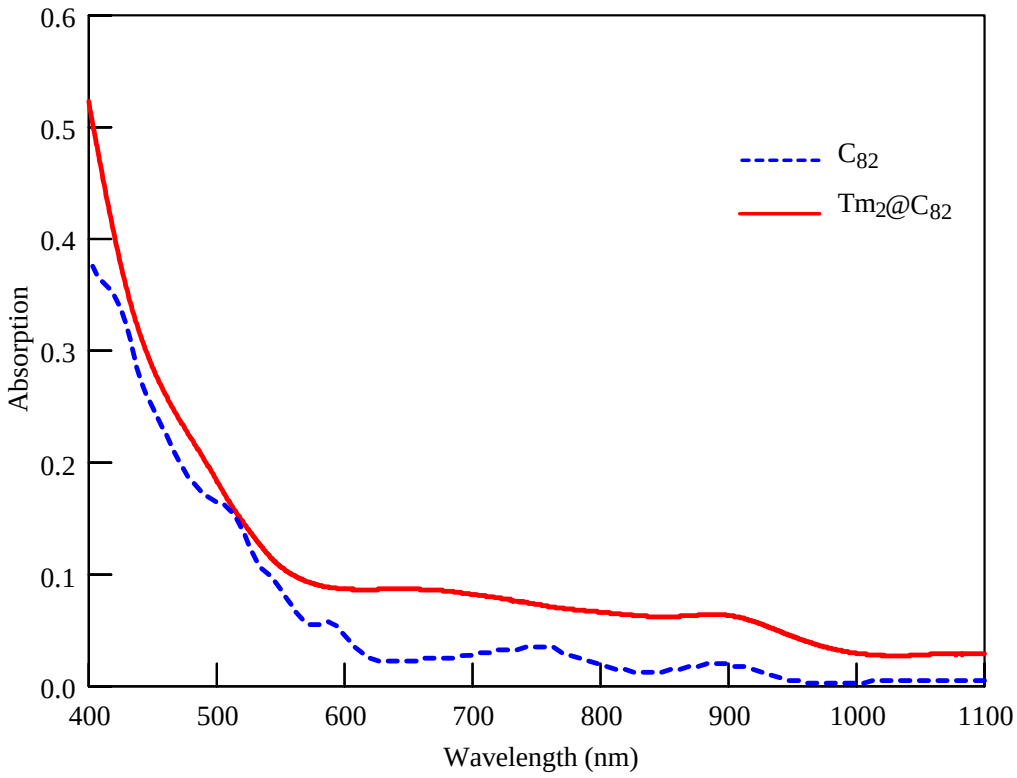

Fig. 3.19 Absorption spectra for $Tm_2@C_{82}$ and C_{82} solutions in CS_2.

spectrophotometer, and recorded the absorptivity at 1064 nm. Figure 3.16 shows the absorption spectra for $Er_2@C_{82}$ (isomer III) and C_{82} solutions in CS_2. The endohedral fullerene shows enhanced absorption features near 650 and 900 nm that result from the charge transfer from the encapsulated atoms to the C_{82} cage. Another distinct feature is the absorption tail at longer wavelengths, and therefore $Er_2@C_{82}$ has a very weak absorption at 1064 nm where the DFWM experiment was made. For the most concentrated solution of 0.32 mg $Er_2@C_{82}$ in 0.8 ml CS_2 (3.0×10^{-4} mol/l) the internal transmittance was greater than 93% at 1064 nm.

3.4 Measurements and interpretation

For each different concentration of $Er_2@C_{82}$ in CS_2, the intensity of the conjugate signal is recorded as a function of the input intensity, both for the solvent and for the solution. In Figure 3.20 is shown the DFWM signal intensity for the CS_2 and the $Er_2@C_{82}$ solution with concentration 2.4×10^{-4} mol/l. The solution has transmittance $T = 94\%$ at 1064 nm. Similar curves were recorded for a total of twenty concentrations of $Er_2@C_{82}$ in CS_2. Both curves obtained are fit to a cubic, $y = ax^3$, by using the least-squares fit method available in the software program TableCurve®. The values of the coefficients a and a_{ref} are used to calculate the third order nonlinear susceptibility of the solution $\chi^{(3)}_{eff}$:

$$\chi^{(3)}_{eff} = \left(\frac{n_0}{n_{ref}}\right)^2 \left(\frac{L_{ref}}{L}\right) \left(\frac{a}{a_{ref}}\right)^{\frac{1}{2}} \frac{\alpha L \exp(\alpha L/2)}{1-\exp(-\alpha L)} \chi^{(3)}_{ref} \qquad (25)$$

For the most concentrated solution, the DFWM signal decreases by 50 % relative to the pure CS_2 solvent, which indicates a very large, negative molecular susceptibility $\gamma(-\omega;\omega,\omega,-\omega)$ for $Er_2@C_{82}$. For comparison, Figure 3.21 shows the cubic fits for CS_2 and $Er_2@C_{82}$ at a lower concentration ($c = 0.9 \times 10^{-4}$ mol/l). In this case, the difference between the DFWM signals for the diluted $Er_2@C_{82}$ solution and that of the pure solvent is not as large as for concentrated solutions of $Er_2@C_{82}$.

For dilute solutions, the effective third order nonlinear susceptibility can be written as

$$\chi^{(3)}_{\text{eff(solution)}} = \chi^{(3)}_{\text{solvent}} + \text{Nf}^4\gamma \tag{26}$$

where N is the number density of solute molecule, $f = \frac{n^2+2}{3}$ is the local field factor, and γ is the second molecular hyperpolarizability of the solute. The value used for the reference CS_2 for the orthogonally polarized beams is $\chi^{(3)}_{\text{xyyx(solvent)}} = 3.6 \times 10^{-13}$ esu[21]. Figure 3.22 displays a linear decrease of $\chi^{(3)}_{\text{eff}}$ with increased concentration. The data is fit to a straight line, and from the slope we calculate the value of the second order hyperpolarizability of $Er_2@C_{82}$, $\gamma_{xyyx}(-\omega;\omega,\omega,-\omega) = 8.65 \times 10^{-32}$ esu. An estimated density of $\rho = 1.7$ g/cm^3 was used to estimate the third order susceptibility for pure film of $Er_2@C_{82}$. The value extrapolated for the film is $\chi^{(3)}_{\text{xyyx film}} = \text{Nf}^4\gamma = 1.1 \times 10^{-9}$ esu, compared to $\chi^{(3)}_{\text{xxxx}} = 7 \times 10^{-12}$ esu[19] for C_{60} and $\chi^{(3)}_{\text{xxxx}} = 12 \times 10^{-12}$ esu[20] for C_{70}, both measured for films at 1064 nm. These values correspond to molecular susceptibilities $\gamma_{\text{xxxx}}(-\omega;\omega,\omega,-\omega)$ of 3×10^{-33} and 5×10^{-34} esu, respectively. For orthogonal polarizations, $\chi^{(3)}_{\text{xyyx}} = 1 \times 10^{-12}$ esu was measured for both C_{60}

and C_{70} films, which corresponds to $\gamma_{xyyx}(-\omega;\omega,\omega,-\omega) = 4 \times 10^{-35}$ esu for C_{60}.

DFWM measurements have also been performed on solutions in CS_2 for the empty-cage fullerenes C_{60}, C_{82} and C_{84}, for concentrations equal to or higher than that of the $Er_2@C_{82}$ solution. As an example, C_{82} is shown in Figure 3.20. The DFWM signal of the empty-cages is indistinguishable from that of the pure solvent, demonstrating that they have a much smaller value for $\gamma_{xyyx}(-\omega;\omega,\omega,-\omega)$ than $Er_2@C_{82}$. The value for $\chi^{(3)}$ for C_{82} is expected to be roughly the same as for C_{60} and C_{70}.

To ensure that the decrease in the DFWM signal is not a consequence of an intensity-induced decreased transmission, we measured the transmission at wavelength 1064 nm for the $Er_2@C_{82}$ and C_{82} solutions at the same intensities as for the DFWM experiment. The backward beam B was used for this measurements. The beam had a radius of 300 μm at the waist and its maximum energy was 320 μJ, thus having a maximum input fluence of 100 $\frac{\text{mJ}}{\text{cm}^2}$. The experimental configuration was similar to the one described in chapter 2 for the optical limiting measurements. The solution displays (Figure 3.23) a linear transmittance with increased input energy, which demonstrates that the decrease observed in the DFWM signal is not due to reverse saturable absorption or two-photon absorption. As seen in the same figure, the empty cage C_{82} also has a linear transmittance at $\lambda = 1064$ nm, for the same range of input energies.

We also performed DFWM measurements in the parallel configuration, in which all beams have the same polarization. Figure 3.24 shows the fits to a cubic for CS_2 and for a low concentration of $Er_2@C_{82}$ solution. We presume that the higher DFWM signal for $Er_2@C_{82}$ is from the thermal contributions to the third

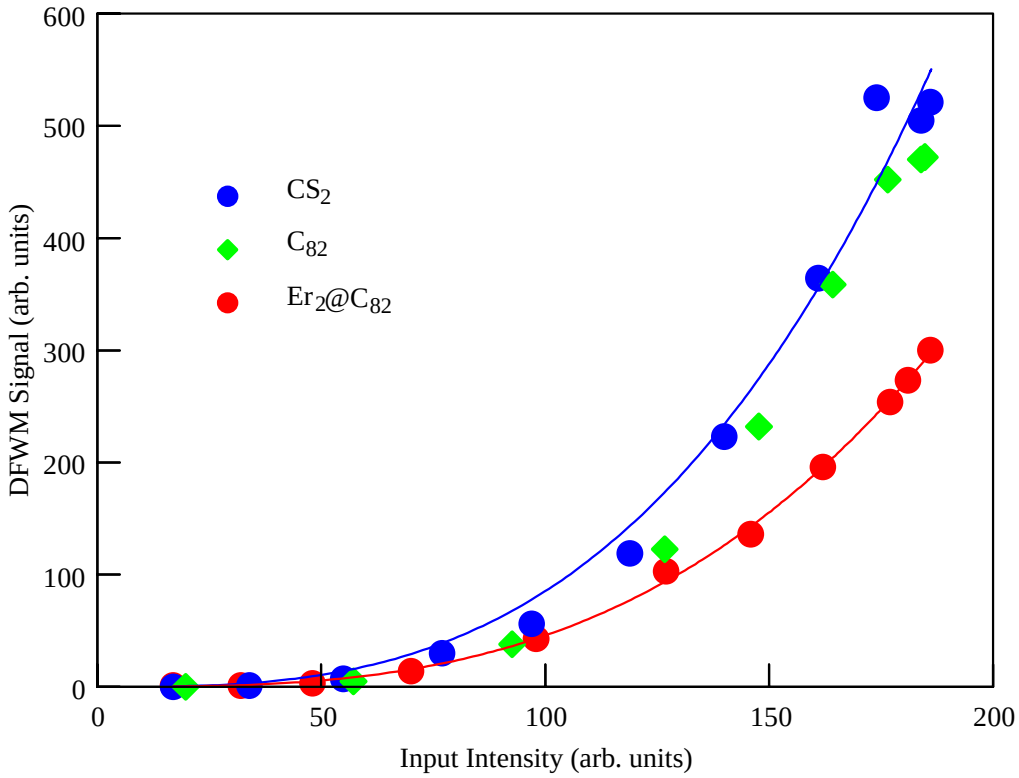

Fig. 3.20 Cubic fit for DFWM signal for $Er_2@C_{82}$, C_{82}, and CS_2. $Er_2@C_{82}$ is at concentration 2.4×10^{-4} mol/l.

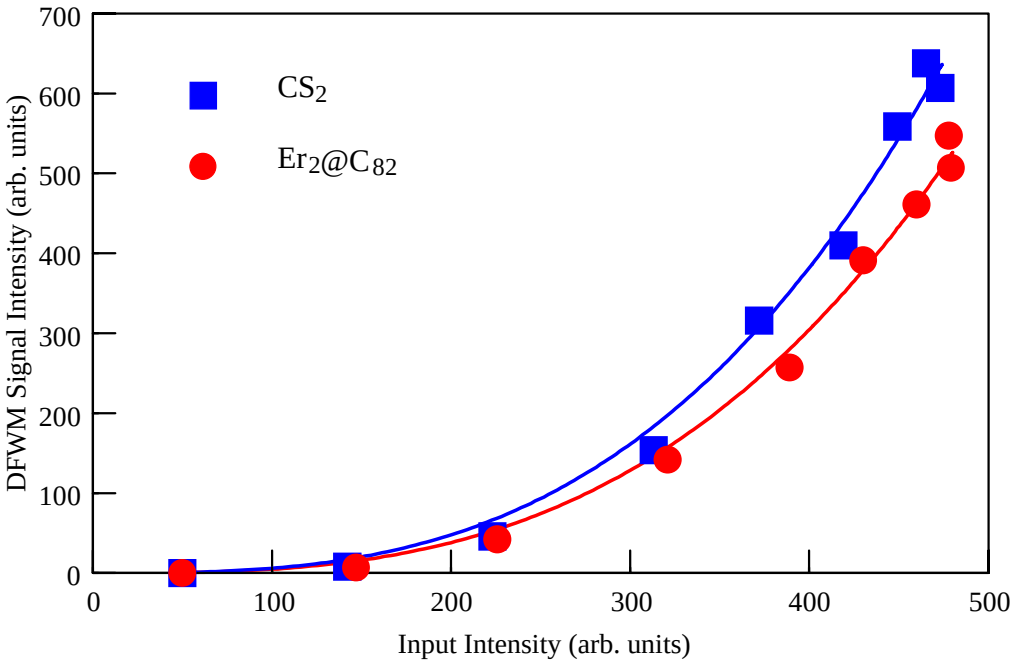

Fig. 3.21 Cubic fit for DFWM signal for $Er_2@C_{82}$ and CS_2. $Er_2@C_{82}$ is at concentration 0.9×10^{-4} mol/l.

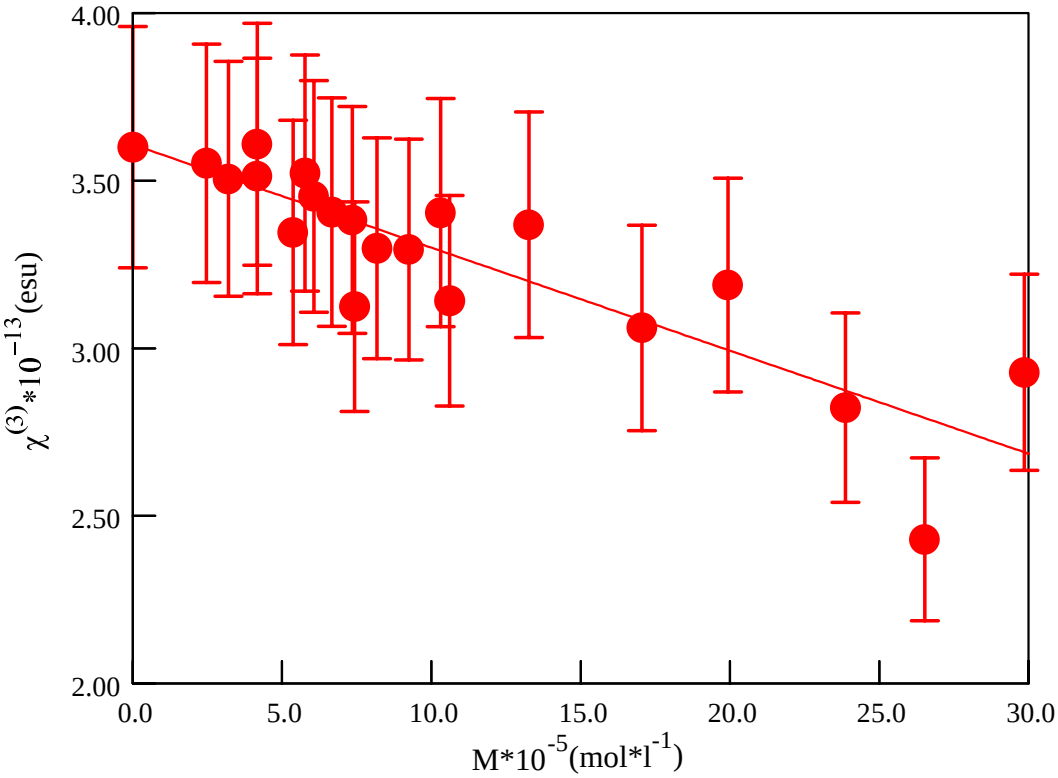

Fig. 3.22 Concentration dependence of $\chi^{(3)}$ for $Er_2@C_{82}$ in CS_2.

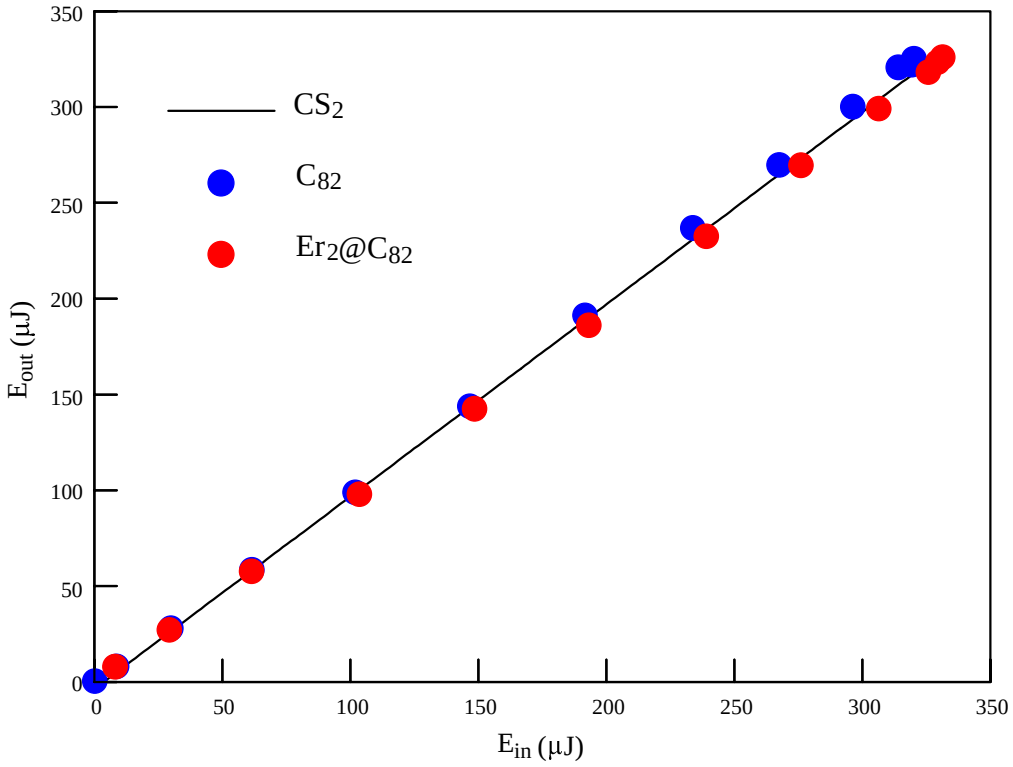

Fig. 3.23 Output energy vs. input energy for $Er_2@C_{82}$ and C_{82} solutions in CS_2.

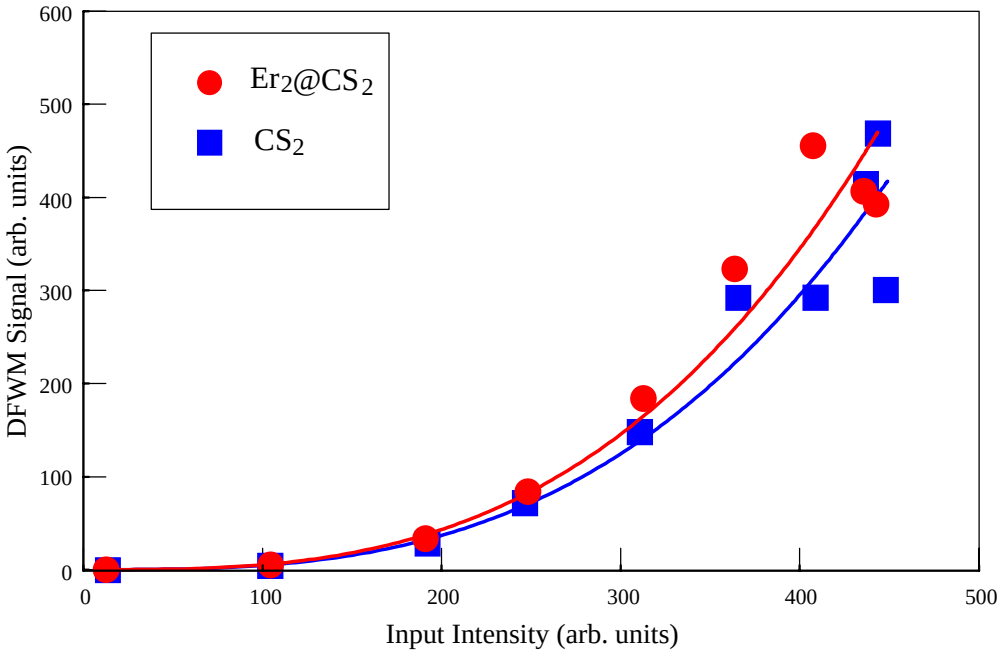

Fig. 3.24 Cubic fit for DFWM signal for $Er_2@C_{82}$ and CS_2. The measurements were made in the parallel configuration, with all beams having the same polarization.

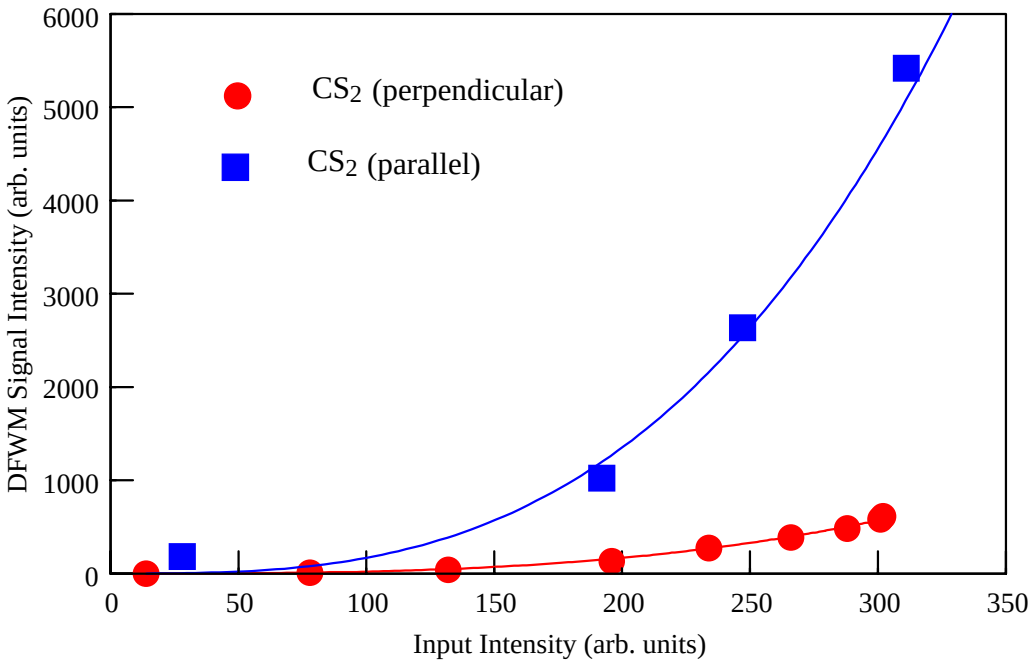

Fig. 3.25 Cubic fit for DFWM signal for CS_2 in the parallel and perpendicular polarization configuration.

order nonlinear susceptibility, $\chi^{(3)}$. Figure 3.25 displays the DFWM signals for the solvent, CS_2, for both configurations, parallel and perpendicular. In the parallel configuration case, the signal was much stronger, by one order of magnitude. Because measurements were taken in different optical alignment conditions, we could not compare the results quantitatively.

3.5 Conclusion

The results of the DFWM experiment show that the endohedral metallofullerene $Er_2@C_{82}$ has a third order nonlinear optical susceptibility $\chi^{(3)}_{xyyx}(-\omega;\omega,\omega,-\omega)$ which is orders of magnitude larger than the empty cage fullerene C_{60}. Our studies demonstrate that an enhancement in $\chi^{(3)}_{xyyx}(-\omega;\omega,\omega,-\omega)$ is caused as a consequence of the charge transfer from the dopant Er atoms to the empty cage C_{82}.

As more material $Er_2@C_{82}$ becomes available, DFWM measurements on films would be more appropriate as a study for potential applications. For the same practical purpose, it would be important to perform wavelength dependence measurements of $\chi^{(3)}_{xyyx}(-\omega;\omega,\omega,-\omega)$ as well as a detailed study at the wavelength 1.54 μm, which is an important telecommunications signal wavelength that also coincides with the wavelength for which Er^{3+} fluorescence occurs. In fact, Erbium-doped glass fiber laser amplifiers are being incorporated into telecommunication networks for direct optical amplification of signals. A question that naturally arises is how do different atoms inside the same cage size affect $\chi^{(3)}_{xyyx}(-\omega;\omega,\omega,-\omega)$ as well as how do different cage sizes with same dopant atoms affect it? With the possibility of synthesizing and purifying a variety of

endohedral metallofullerenes in large quantities, these questions could be answered in the near future.

References

[1] Robert W. Boyd, Nonlinear optics, Academic Press (1992).

[2] H.J. Eichler, P. Gunter, D.W. Pohl, Laser-induced dynamic gratings, Springer-Verlag (1986).

[3] Daniel J. McGraw, A.E. Siegman, G.M. Wallraff, and R.D. Miller, Appl. Phys. Lett. **54**, 1713 (1989).

[4] P.A. Fleitz, R.L. Sutherland, L.V. Natarajan, T. Pottenger, and N.C. Fernelius, Optics Letters **17**, 716 (1992).

[5] Richard L. Sutherland, Handbook of nonlinear optics, Optical Engineering **52**, (1996).

[6] Robert A. Fisher, Optical phase conjugation, Academic Press (1983).

[7] K. Kikuchi, Y. Nakao, S. Suzuki, and Y. Achiba, J. Am. Chem. Soc. **116**, 9367 (1994).

[8] D. S. Bethune, R. D. Johnson, J. R. Salem, M. S. de Vries, and C. S. Yannoni, Nature **366**, 123 (1993) and references within.

[9] H.C. Dorn, S. Stevenson, P. Burbank, Z. Sun, T. Glass, K. Harich, P.H.M. Van Loosdrecht, R.D. Johnson, R. Beyers, J.R. Salem, M.S. De Vries, C.S. Yannoni, C.H. Kiang, and D.S. Bethune, Materials Research Society Symposium Proceedings **359**, 123 (1995).

[10] R. D. Johnson, M. S. de Vries, J. Salem, D. S. Bethune, and C. S. Yannoni, Nature **355**, 239 (1992).

[11] C. S. Yannoni, M. Hoinkis, M. S. de Vries, D. S. Bethune, J. R. Salem, M. S. Crowder, R. D. Johnson, Science **256**, 1191 (1992).

[12] R. Beyers, C-H. Klang, R. D. Johnson, J. R. Salem, M. S. de Vries, C. S. Yannoni, D. S. Bethune, H. C. Dorn, P. Burbank, K. Harich, and S. Stevenson, Nature **370**, 196 (1994).

[13] Roger M. Macfarlane, Georg Wittman, Paul H. M. van Loosdrecht, Mattanjah de Vries, Donald S. Bethune, Steve Stevenson, and Harry C. Dorn, Phys. Rev. Lett. **79**, 1397 (1997).

[14] X. Ding, J. M. Alford, and J. C. Wright, Chem. Phys. Lett. **269**, 72 (1997).

[15] Gerhard Heinrich Dieke, Spectra and Energy Levels of rare Earths Ions in Crystals, Interscience Publishers (1968).

[16] J. R. Heflin et al., Phys. Rev. A **45**, 4233 (1991).

[17] D. C. Rodenberger, J. R. Heflin, and A. F. Garito, Nature **359**, 309 (1992).

[18] D. C. Rodenberger, J. R. Heflin, and A. F. Garito, Phys. Rev. A **51**, 3234 (1995).

[19] Z.H. Kafafi, J.R. Lindle, R.G.S. Pong, F.J. Bartoli, L.J. Lingg, and J. Milliken, Chem. Phys. Lett. **188**, 492 (1992).

[20] J. R. Lindle, R. G. S. Pong, F. J. Bartoli, and Z. H. Kafafi, Phys. Rev. B **48**, 9447 (1993).

[21] R. W. Hellwarth, Prog. in Quant. Electr. **5**, 1 (1977).